Optica Applicata, Vol. LVI, No. 1, 2026
DOI: 10.37190/oa/215065

High power and high thermal performance multi-junction VCSEL with n-type oxide layers and composition gradient spacer layers

YUFEI WANG[1,2], YIBO YANG[1,2], LEI YU[1,2], JIAOQING PAN[1,2,3], YANMEI SU[1,2], YEJIN ZHANG[1,2,3,*]

[1] State Key Laboratory of Optoelectronic Materials and Devices, Institute of Semiconductors, Chinese Academy of Sciences, Beijing 100083, China

[2] Center of Materials Science and Optoelectronic Engineering, University of Chinese Academy of Sciences, Beijing 100049, China

[3] Xinchen Semiconductor Co., Ltd., Suzhou, China

[*]Corresponding author: yjzhang@semi.ac.cn

The self-heating effect of multi-junction vertical cavity surface emitting lasers (MJ VCSELs) under continuous current injection seriously affects their output performance and durability. In this study, we designed and simulated a multi-junction bottom-emitting VCSEL structure. By adopting the n-type oxide layers and the component gradient spacer layers, the optical output performance of the device under continuous current injection was effectively improved. Compared with the traditional MJ VCSEL structure, the designed device can achieve a peak power increase of more than 30 mW and an 18% improvement in electro-optical power conversion efficiency (PCE) without changing the oxidation aperture. Meanwhile, this new type of MJ VCSEL shows good adaptability to the increase of environmental temperature. Even at an ambient temperature of 80 °C, it can still achieve comparable performance to the traditional structure of MJ VCSEL at room temperature. The results of this study indicate that the structure we designed is promising for the achievement of high-performance MJ VCSELs.

Keywords: multi-junction VCSEL, thermal performance, oxide layer, composition gradient.

1. Introduction

Vertical cavity surface emitting lasers (VCSELs) have been widely applied in optical communication, consumer electronics, and 3D sensing due to their advantages of compactness, low threshold current, simple manufacturing process and high beam quality [1-4]. However, compared with edge-emitting lasers (EELs), VCSELs can only achieve lower optical power in general due to their smaller active region volume with current injection, which limits their application in long-distance data transmission and sensing. Although high-power optical output can be achieved through the large-scale on-chip integration of 2D VCSEL arrays, severe thermal crosstalk can affect their power stability and beam quality [5].

Another promising technology for improving VCSEL power is the multi-junction VCSEL (MJ VCSEL). In MJ VCSELs, electrons can recombine in multiple active regions through the tunnel junction, thereby significantly improving the internal quantum efficiency, power density and power conversion efficiency (PCE) [6]. So far, there have been numerous reports on high-performance MJ VCSELs in industrial fields and scientific research. For instance, Lumentum reported a 5-junction VCSEL array that reached a peak power of 800 W under a 200 A pulsed current injection [7]. Everbright Photonics's 8-junction 940 nm VCSEL array realized a PCE of 59.7%, a slope efficiency of 8.3 W/A, and a maximum power density up to 1800 W/mm2 [8]. Yao Xiao et al. reported 15-junction VCSELs that can achieve a maximum efficiency of 74% at room temperature under nanosecond driving current [9]. However, at present, there are still relatively few studies on the optimization of thermal characteristics of multi-junction VCSELs.

Compared with single-junction VCSELs, MJ VCSELs can achieve a significant improvement in quantum efficiency due to the multiple recombination of carriers. Whereas their peak power usually cannot increase proportionally. The main reason is that the multiple active regions, tunnel junctions, and spacer layers contained in the resonant cavity increase the series resistance of the device. As the injected current increases, the lattice temperature of MJ VCSELs rise much faster than that of single-junction devices [10]. The rapid increase of lattice temperature leads to a quick decline of material gain, resulting in the quick saturation of output power as the current increases [11]. Unfortunately, this problem intensifies as the number of active regions increases. Therefore, MJ VCSEL typically can only be pumped by a pulsed power supply with a low duty cycle when facing high current injection, which limits its application field. Based on this, if the structure of MJ VCSELs can be optimized to improve the thermal performance and increase the thermal rollover current, the peak output power can be expected to increase significantly.

Existing researches on improving thermal performance in VCSELs mainly include: improving the heat dissipation of VCSEL arrays by optimizing array layout [12-14], improving thermal management through packaging technology [15], using electron blocking layer to reduce the heat generation caused by non-radiative recombination [16], using wavelength detuning technology to enhance the mode gain of VCSELs at high ambient temperature [17] and so on. In addition, for the thermal characteristic optimization of multi-junction VCSELs, it has been proved that reducing the number of oxide layers can lower the temperature of the active regions [11]. However, this structure leads to an increase in the threshold current and a decrease in PCE due to the lateral diffusion of current at the heavily doped tunnel junctions.

In this paper, we designed and simulated a novel bottom-emitting MJ VCSEL structure. By using n-doped oxide layers and AlGaAs spacer layers with a graded Al composition between each two active regions, we effectively reduced the heat generation, increased the thermal rollover current and slop efficiency simultaneously, thus achieving a significantly higher peak output power and PCE compared with the conventional MJ VCSELs.

2. Device structure design and simulation

In this study, three pairs of 6 nm-$In_{0.22}Ga_{0.78}As$/8 nm-$GaAs_{0.92}P_{0.08}$ multiple quantum wells (MQWs) are used for each active region. The emission wavelength of the designed device is 980 nm. Since GaAs substrate has weak absorption for 980 nm infrared light, the VCSEL can be designed as a bottom-emitting structure, which can improve the heat dissipation efficiency owing to the direct connection of p-DBRs and heat sink by flip -chip bonding [18].

As shown in Fig. 1, three types of 3-junction VCSELs with different device structures are designed for comparison. All three structures adopt the same active regions. By carefully adjusting the thickness of each spacer layer, all the active regions are aligned with the antinode of the standing wave, while the tunnel junctions and the oxide

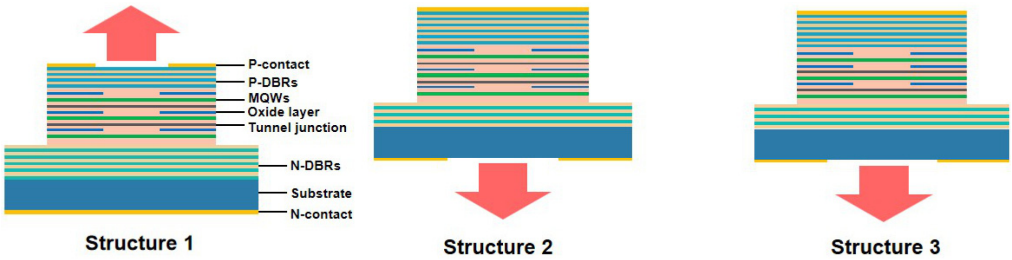

Fig. 1. Schematic diagram of three different structures of MJ VCSELs.

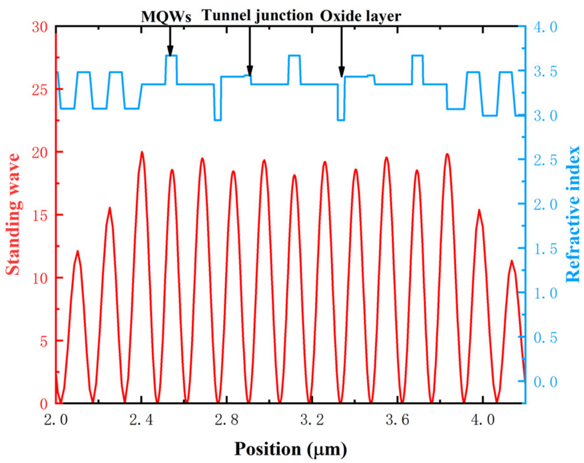

Fig. 2. Diagram of standing wave and refractive index near the active regions.

layers are positioned at the node of the standing wave in the resonance cavity as shown in Fig. 2, which can maximize the optical gain while reducing the free carrier absorption loss [19]. The p-side and n-side of the tunnel junctions of all three structures are heavily doped with doping concentrations of 1×10^{20} and 4×10^{19} cm^{-3}, respectively. The devices employ oxide layers to realize the restriction of the current flow. Considering the influence of the oxide aperture size on the threshold current, the uniformity of electrical injection, and the heating rate of the active region, we chose 12 μm as the diameter of the oxide aperture for all the devices in this paper.

Structure 1 in Fig. 1 is a conventional top-emission VCSEL. Based on the calculation of the transfer matrix [20], the top and bottom DBRs of the device are composed of 16.5 pairs of $Al_{0.2}Ga_{0.8}As$/GaAs and 30 pairs of $Al_{0.9}Ga_{0.1}As$/GaAs materials with a thickness of 1/4 optical wavelength, respectively, to achieve an appropriate reflectance. The oxide layers between the active regions are set in the p-doped region of the spacer layers. On the contrary, structure 2 is designed as a bottom-emission structure. The materials design inside the resonant cavity remains the same as those in structure 1, while changing the p-DBRs and n-DBRs to 30 pairs of $Al_{0.9}Ga_{0.1}As$/GaAs and 16 pairs of $Al_{0.2}Ga_{0.8}As$/GaAs materials respectively. The only difference between structures 3 and 2 is that the oxide layers between the active regions are set in the n-doped regions of the spacer layers instead of the p-doped regions. We keep the p-type oxide layer at the bottom of the p-DBRs of structure 3 for the consideration of forming a good limitation of injected current in the top MQWs. Specific epitaxial structures of the regions between each two active regions of the devices are listed in Tables 1 and 2.

We performed simulations of the optical and temperature characteristics of the three VCSELs under continuous electrical injection using Pics3d software. The simulation considers the impact of device heating on performance under different current injections. The environmental temperature is set to 300 K, with the n-electrodes of structure 1 and the p-electrodes of structures 2 and 3 connected to a copper heat sink. The contact position between the device and the heat sink is considered to be at a constant temperature same as the environment. On the other side, heat dissipation is carried out through metal electrodes. The contact between the electrodes and materials is defined as ideal ohmic contact, thus ignoring the influence of contact resistance. The ther-

T a b l e 1. Detailed parameters of the regions between each two MQWs of structures 1 and 2.

	Material	Doping concentration [cm^{-3}]	Thickness [nm]
Active region 1	$In_{0.22}Ga_{0.78}As/GaAs_{0.92}P_{0.08}$	0	6/8
Center spacer 1	n-$Al_{0.42}Ga_{0.58}As$	4×10^{18}	178
Tunnel junction	n-$Al_{0.28}Ga_{0.03}As$	4×10^{19}	15
	p-$Al_{0.28}Ga_{0.72}As$	1×10^{20}	15
Center spacer 2	p-$Al_{0.3}Ga_{0.7}As$	4×10^{18}	110
Oxide layer	p-$Al_{0.97}Ga_{0.03}As$	4×10^{18}	30
Center spacer 3	p-$Al_{0.42}Ga_{0.58}As$	4×10^{18}	178
Active region 2	$In_{0.22}Ga_{0.78}As/GaAs_{0.92}P_{0.08}$	0	6/8

Table 2. Detailed parameters of the regions between each two MQWs of structure 3.

	Material	Doping concentration [cm^{-3}]	Thickness [nm]
Active region 1	$In_{0.22}Ga_{0.78}As/GaAs_{0.92}P_{0.08}$	0	6/8
Center spacer 1	n-$Al_{0.42}Ga_{0.58}As$	4×10^{18}	178
Oxide layer	n-$Al_{0.97}Ga_{0.03}As$	4×10^{18}	30
Center spacer 2	n-$Al_{0.3}Ga_{0.7}As$	4×10^{18}	110
Tunnel junction	n-$Al_{0.28}Ga_{0.03}As$	4×10^{19}	15
	p-$Al_{0.28}Ga_{0.72}As$	1×10^{20}	15
Center spacer 3	p-$Al_{0.42}Ga_{0.58}As$	4×10^{18}	178
Active region 2	$In_{0.22}Ga_{0.78}As/GaAs_{0.92}P_{0.08}$	0	6/8

mal conductivity of the ternary alloy materials $A_xB_{1-x}C$ is calculated by the following equation [21]:

$$K(x) = \frac{1}{xW_{AC} + (1-x)W_{BC} + x(1-x)C_{A-B}} \tag{1}$$

where W_{AC} and W_{BC} are the thermal resistances of material AC and BC, respectively, and C_{A-B} represents the contribution of lattice disorder. The relevant parameters of the materials used in the simulation such as AlGaAs, InGaAs, and GaAsP are taken from the reference [21]. For multilayer thin film materials such as DBRs and MQWs, define their anisotropic thermal conductivities as [22]:

$$K_H = \frac{d_1K_1 + d_2K_2}{d_1 + d_2} \tag{2}$$

$$K_V = \frac{d_1 + d_2}{d_1/K_1 + d_2/K_2} \tag{3}$$

where K_H and K_V are the average thermal conductivities of the periodic structures in the horizontal and vertical directions. K_1 and K_2 are the thermal conductivities of the

Table 3. Thermal conductivity of each material used in the simulation.

Layers	Material	Effective thermal conductivity [W/m·K]
p-DBR	$GaAs/Al_{0.9}Ga_{0.1}As$	K_H: 33.9; K_V: 0.9
Oxide layer	$Al_{0.97}Ga_{0.03}As$	48.4
MQWs	$In_{0.22}Ga_{0.78}As/GaAs_{0.92}P_{0.08}$	K_H: 17.3; K_V: 11.7
Spacer layers	$Al_{0.42}Ga_{0.58}As$	10.5
	$Al_{0.3}Ga_{0.7}As$	11.6
Tunnel junction	n^+/p^+: $Al_{0.28}Ga_{0.72}As$	12
n-DBR	$GaAs/Al_{0.8}Ga_{0.2}As$	K_H: 29.3; K_V: 22.4
Substrate	GaAs	45

two layers, and d_1 and d_2 are their thicknesses, respectively. The detailed thermal conductivity parameters of the materials used in the simulation are listed in Table 3.

The simulation results for the power-current-voltage (*P-I-V*) characteristics, PCE, and the relationship between the maximum lattice temperature and the injection current for the three device structures are shown in Fig. 3. It can be seen that the bottom-emitting VCSEL with n-type middle oxide layers exhibits the highest slope efficiency, peak power and PCE. Additionally, it has the smallest differential resistance and the slowest increase in lattice temperature with the increase of injection current, resulting in the highest thermal rollover current among the three devices. Meanwhile, the threshold current is just slightly greater than that of devices 1 and 2 with p-type middle oxide layers. It is noteworthy that when the current exceeds the thermal rollover current, the maximum lattice temperatures in the active regions of all three structures will exceed 450 K as shown in Fig. 3. This may lead to stress release due to lattice mismatch between InGaAs quantum wells and GaAsP barriers, resulting in lattice defects. In addition, stress accumulation at the edge of the oxide layer caused by high temperatures may also form dislocations in the active region, thereby affecting the performance and lifespan of the device. In the actual operation of the device, excessive continuous current injection should be avoided.

The superior performance of structure 2 compared to structure 1 is primarily attributed to the better heat dissipation capability of the bottom-emitting structure which has been confirmed by existing studies [23]. The performance advantages of structure 3 over structure 2 can be attributed to the following two reasons. One is that the adoption of n-type oxidation layers significantly increases the proportion of the n-type region between each two active regions, as clearly shown in the epitaxial structure listed in Table 2.

Since electrons have a smaller effective mass and a much higher mobility compared to holes, the resistance of the n-type region is much lower than that of the p-type region. In addition, the free carrier absorption in the p-type region is usually significantly higher than that in the n-type region [18]. The decreased proportion of the p-doped region

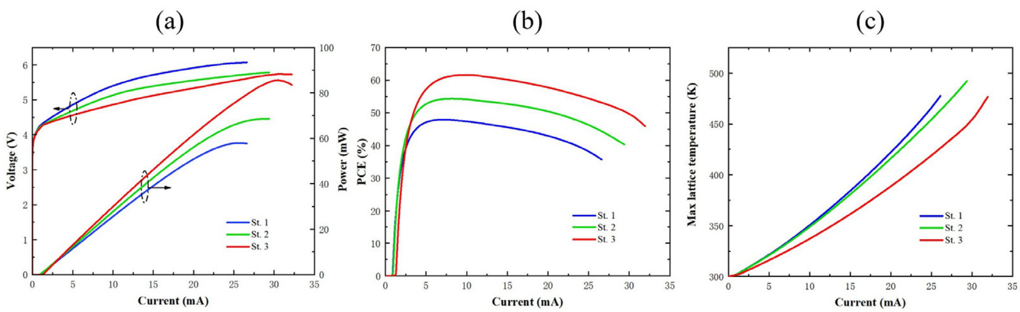

Fig. 3. Simulation results of the (a) *P-I-V* (b) PCE and (c) lattice temperature characteristics of VCSELs with three different structures.

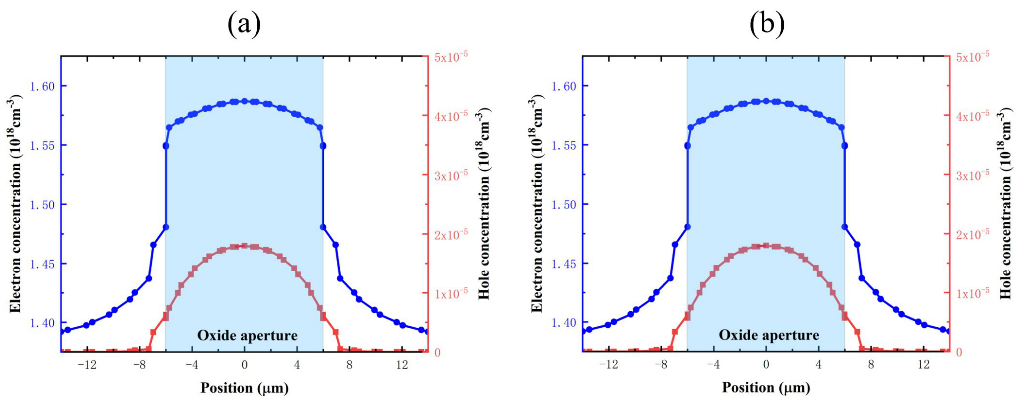

Fig. 4. Carrier distribution of the spacer layer adjacent to the (a) n-type oxide layer and (b) p-type oxide layer.

reduces the series resistance and free carrier absorption between active regions, thereby minimizing the generation of heat and the loss of light power under the same injection current. The second one is that the n-type oxidation apertures have a higher conductivity, leading to a more uniform lateral distribution of carriers. In contrast, the relatively higher resistance of p-type oxide apertures makes carriers mainly concentrate in the central region of the oxide apertures which can be seen in Fig. 4.

The uniform horizontal carrier distribution resulting from the n-doped oxide aperture increases the volume of the active regions with high carrier concentration, thus increasing the radiative recombination efficiency. Meanwhile, compared with the VCSEL with p-type middle oxide layers, the slightly lower current density in the central region of the oxide aperture also explains the slight increase in its threshold current as can be seen in Fig. 3. Additionally, the enhanced uniformity of carrier injection leads to a more uniform distribution of heat in the horizontal direction. Figure 5(a) shows the thermal distributions of three structures at the same maximum lattice temperature, and Fig. 5 (b) illustrates their lateral temperature distributions of the middle active regions. As clearly seen, for structures 1 and 2 with p-type oxide layers, there is no significant difference in the lateral temperature distribution of the active regions within the oxide apertures. In contrast, for structure 3 with n-type intermediate oxide layers, the lattice temperature distribution presents better uniformity, which is consistent with the carrier distributions shown in Fig. 4. Notably, although VCSEL with structure 3 shows a higher average temperature in the oxide aperture in Fig. 5, this is achieved at a higher injection current where its power apparently exceeds that of VCSELs with structures 1 and 2. The combination of higher internal quantum efficiency, lower resistance, and better heat dissipation results in VCSEL of structure 3 can reach a higher slope efficiency and thermal rollover current, ultimately leading to the improvements in its peak power and PCE.

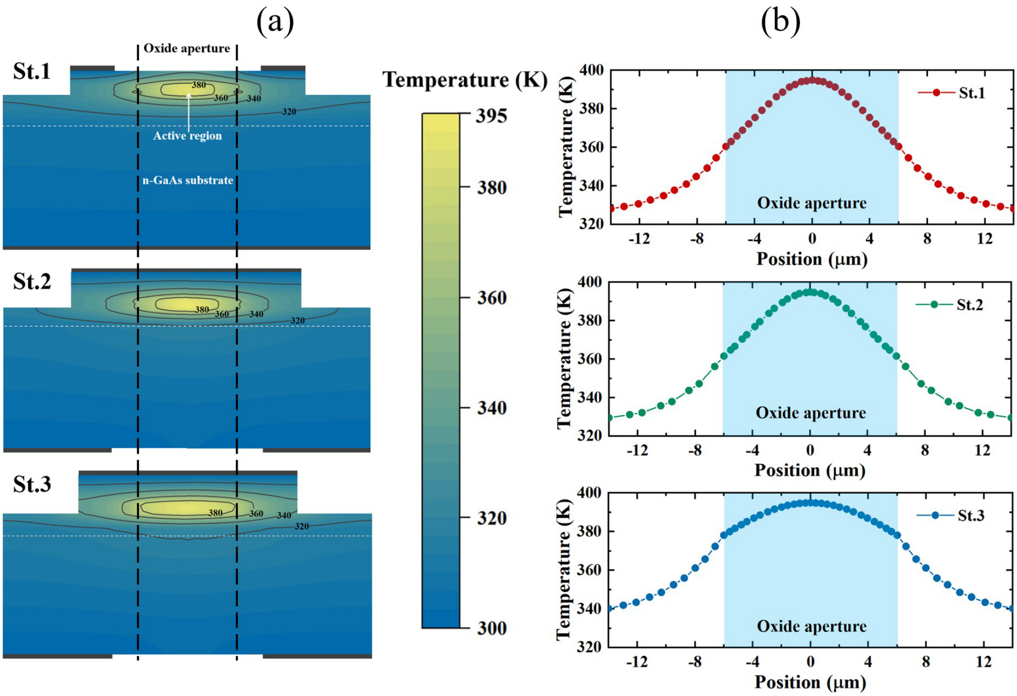

Fig. 5. (a) 2D lattice temperature distributions of MJ VCSELs with the three structures and (b) 1D lateral temperature distributions of the middle MQWs of the three VCSELs at the same maximum temperature.

3. Device structure optimization

To further enhance the performance of the designed device, we optimized the spacer layer based on structure 3 by replacing the fixed-composition middle spacer layer in contact with the active region by AlGaAs material with a gradient Al composition as structure 4. The optimized epitaxial structure between the active regions is listed in Table 4. The changes in Al composition affect the refractive index of the AlGaAs material, and thereby influenc the equivalent cavity length of the VCSEL [24]. Here, we finely tuned the thickness of the spacer layers to ensure that the center wavelength aligns with 979 nm with a current injection near the threshold, and thereby the impact of gain differences was excluded. The bandgap of $Al_xGa_{1-x}As$ material with different Al compositions can be expressed as [25]:

$$E_g(Al_xGa_{1-x}As) = xE_g(AlAs) + (1-x)E_g(GaAs) - x(1-x)(-0.127 + 1.31x) \quad (4)$$

where the bandgap of AlAs and GaAs at room temperature are approximately 2.34 and 1.42 eV, respectively.

Apparently, the bandgap of AlGaAs materials increases as the increase of Al composition, leading to a rise in the electron potential barrier and thereby suppressing elec-

T a b l e 4. Detailed parameters of the regions between each two MQWs of structure 4.

	Material	Doping concentration [cm^{-3}]	Thickness [nm]
Active region 1	$In_{0.22}Ga_{0.78}As/GaAs_{0.92}P_{0.08}$	0	6/8
Center spacer 1	n-$Al_{0.42}Ga_{0.58}As$-$Al_{0.3}Ga_{0.7}As$	4×10^{18}	176
Oxide layer	n-$Al_{0.97}Ga_{0.03}As$	4×10^{18}	30
Center spacer 2	n-$Al_{0.3}Ga_{0.7}As$	4×10^{18}	110
Tunnel junction	n-$Al_{0.28}Ga_{0.03}As$	4×10^{19}	15
	p-$Al_{0.28}Ga_{0.72}As$	1×10^{20}	15
Center spacer 3	p-$Al_{0.28}Ga_{0.72}As$-$Al_{0.42}Ga_{0.58}As$	4×10^{18}	176
Active region 2	$In_{0.22}Ga_{0.78}As/GaAs_{0.92}P_{0.08}$	0	6/8

tron leakage from the active regions. Nevertheless, the heterojunction formed between AlGaAs materials with different Al compositions is of type-I, which means the barrier for holes will also increase accordingly, thus affecting the hole injection efficiency [26].

To avoid the formation of additional hole barriers, we keep the spacer layer's Al component the same as that of structure 3 on the side adjacent to the active region and gradually reduce the Al component to 0.28 on the other side, which is the same as the tunnel junctions. Figure 6 shows the band diagram near the active region, indicating that the gradient spacer layer can create a high potential barrier of 0.54 eV for electrons, while it has almost no additional blocking effect on holes. This ensures the effective blocking of electron leakage while maintaining efficient hole injection.

Compared with the fixed-composition spacer layers, the composition gradient spacer layers have a lower Al composition same as the tunnel junction material on the side away from the active region, resulting in the removal of abrupt heterojunction and the smaller energy gaps between the conduction band/valence band and the electron/hole

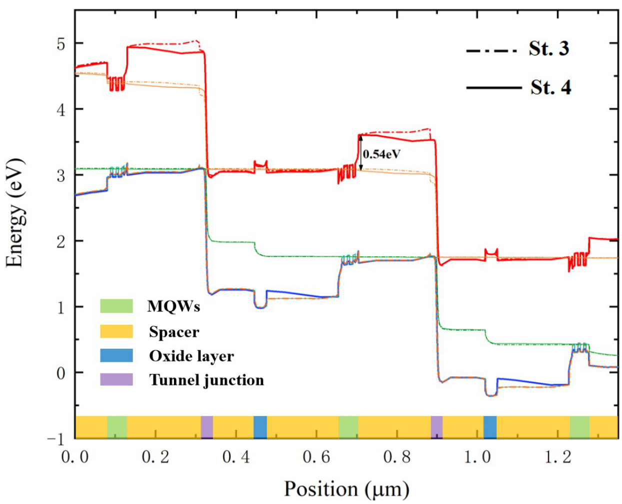

Fig. 6. Energy band diagram of the structures 3 and 4 with an injection current of 4 mA.

quasi-Fermi levels, which implies that the composition gradient spacer layer contains a higher average carrier concentration. The higher carrier concentration in the spacers can ensure the efficient injection of carriers in the active regions. High carrier concentration near the tunnel junction also effectively improves the tunneling current density and reduces the resistivity as well.

Additionally, the composition gradient spacer layer can also affect the optical confinement factor of the active regions. The refractive index of AlGaAs material will decrease with the increase of Al components. The Al component in the structure 4 spacer layer decreases outward from the active region. This gradual change of the Al component forms a refractive index distribution that increases from the active region to the tunnel junctions. This refractive index distribution form can guide the optical field to diffuse into the spacer layers, thus reducing the optical confinement factor of the active regions. The relationship between the internal loss α_i and the optical confinement factor Γ follows [27]:

$$\alpha_\mathrm{i} = \sum_q \alpha_q = \sum_q \Gamma_q (\sigma_n n_q + \sigma_p p_q) \tag{5}$$

where α_q and Γ_q represent the internal loss and optical confinement factor of the q-th region, σ_n and σ_p are the scattering cross-sections of the electrons and holes. n_q and p_q are the carrier concentrations of electrons and holes.

According to the equation, the decrease of the optical confinement factor can reduce the free-carrier absorption in the active region. Although the expansion of the light field into the spacer layers will also cause an increase in the free-carrier absorption in the spacer layers, since the carrier concentration in the spacer layer is much lower than that in the active region, the impact of its internal loss can be ignored relatively.

The relationship between the slope efficiency (SE) and loss of semiconductor lasers follows:

$$\mathrm{SE} = \frac{h\nu}{q} \eta_\mathrm{i} \frac{1}{1 + \alpha_\mathrm{i}/\alpha_\mathrm{m}} \tag{6}$$

where h is the Planck constant, ν represents the laser frequency, q stands for electron charge, η_i is the carrier injection efficiency, α_i and α_m are internal loss and mirror loss, respectively. It can be seen that the reduction of internal loss helps to improve the slope efficiency of the device.

To verify the improvement of device performance by the component gradient spacer layer, we conducted simulation of the VCSEL with structure 4 under continuous current injection. Figure 7 presents a comparison of the *P-I-V* characteristics of the VCSELs with structures 4 and 3 at room temperature (300 K). As shown, the optimized device exhibits a higher slope efficiency and thermal rollover current, enabling it to achieve a higher peak power of 92 mW and PCE of 66%.

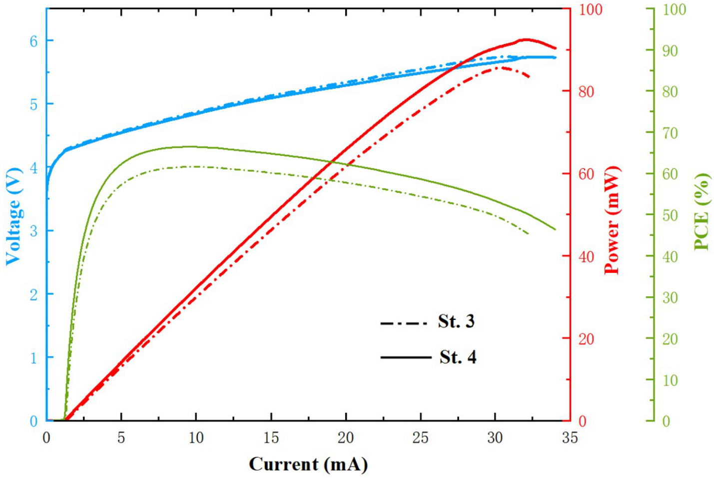

Fig. 7. The *P-I-V* characteristic diagram of the VCSELs of structures 3 and 4.

Based on the optimized device structure, we further performed simulations to evaluate the performance at different ambient temperatures. As the temperature rises, the carrier leakage in the active region increases due to the increase of the thermal motion of carriers and the decrease of potential barriers [28]. This leads to an increase in the threshold current, and a decrease in the slope efficiency, peak optical power, and PCE. Meanwhile, the voltage value at the same current also slightly decreases, which is mainly due to the decrease in resistivity caused by the increase in carrier concentration as the temperature rises. As shown in the results in Fig. 8, when the temperature rises from 20 to 100 °C, the threshold current of the device increases from 1.3 to 2.42 mA, the slope efficiency gradually decreases from 3.6 to 2.9 mW/mA, and the peak power also decreases by more than 50 mW. However, even at a high ambient temperature of 80 °C, the device can still achieve a maximum optical power of 49 mW and an PCE of over 50%, which is comparable to the performance of structure 1 at room temperature, demonstrating that the device designed in this work exhibits excellent high-temperature operation characteristics.

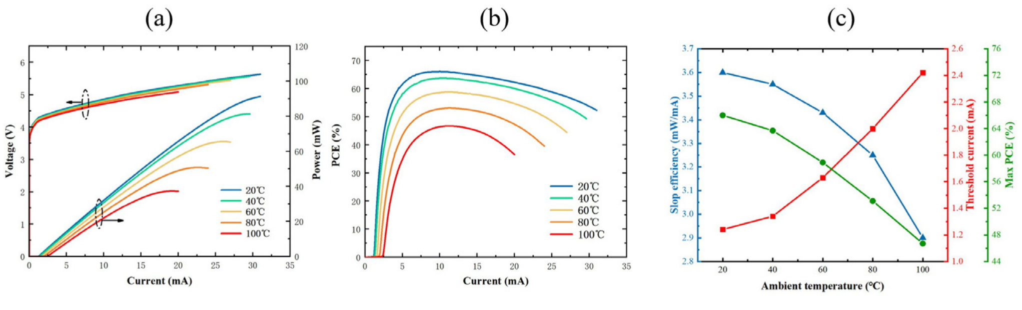

Fig. 8. (a) *P-I-V*, (b) PCE and (c) slop efficiency, threshold current, and max PCE of the VCSELs of structure 4 at different ambient temperatures.

4. Conclusion

In this paper, the optical and thermal performance of MJ VCSELs under continuous current injection is optimized by adjusting the materials and structure of the regions between the MQWs. The results show that the device with n-type middle oxide layers and Al composition gradient spacer layers exhibits great optical and thermal properties. Compared with the conventional top-emission MJ VCSEL structure, the new structure successfully increased the thermal inversion current, peak power and PCE owing to the more uniform carrier injection, lower resistivity, and better heat dissipation. Furthermore, the simulation results of the device performances under different ambient temperatures show that the device structure designed in this work still has great applicability in high-temperature environments. It can be predicted that the power and efficiency of the device can be further enhanced by increasing the number of active regions. In conclusion, this work provides a practical method for the optimization of MJ VCSEL from the perspective of structural design, which is helpful for the fabrication of high-performance MJ VCSELs.

Acknowledgements
This work was supported in part by the National Key R&D Program of China (2022YFB2804503), and National Natural Science Foundation of China (62090053 and 62274153).

References

[1] TONG H., WEI Z., TONG C., WANG Y., MENG B., WANG L., *High-speed 850 nm vertical-cavity surface -emitting lasers with multilayer oxide aperture*, 2022 IEEE 14th International Conference on Advanced Infocomm Technology (ICAIT), Chongqing, China, 2022: 216–219. https://doi.org/10.1109/ICAIT56197.2022.9862777

[2] ZHANG J., ZHENG W., LIU A., *Polarized vertical-cavity surface-emitting laser arrays with asymmetrical structures for three-dimensional sensing with polarization imaging*, IEEE Journal of Quantum Electronics, **59**(5), 2023: 2400408. https://doi.org/10.1109/JQE.2023.3295399

[3] LI N., HO C.P., XUE J., LIM L.W., CHEN G., FU Y.H., LEE L.Y.T., *A progress review on solid-state LiDAR and nanophotonics-based LiDAR sensors*, Laser & Photonics Reviews, **16**(11), 2022: 2100511. https://doi.org/10.1002/lpor.202100511

[4] KOYAMA F., *Advances and new functions of VCSEL photonics*, Optical Review, **21**(6), 2014: 893–904. https://doi.org/10.1007/s10043-014-0142-6

[5] DONG L., GU X., HU S., KOYAMA F., *Densely packed 1.1 μm band vertical cavity surface emitting laser array for co-packaged optics*, Japanese Journal of Applied Physics, **61**(SK),2022, SK1011. https://doi.org/10.35848/1347-4065/ac64e3

[6] KNODL T., GOLLING M., STRAUB A., JAGER R., MICHALZIK R., EBELING K.J., *Multistage bipolar cascade vertical-cavity surface-emitting lasers: Theory and experiment*, IEEE Journal of Selected Topics in Quantum Electronics, **9**(5), 2003: 1406–1414. https://doi.org/10.1109/JSTQE.2003.819484

[7] XIE S., ZHAO G., YANG J., KALAGARA H., LI Y., LASSISE M., CHAI S., PETERS M., SKIDMORE J., *High -Power and High-Speed Multi-Junction VCSEL Arrays for Automotive LiDAR*, 2022 IEEE Photonics Conference (IPC), IEEE: Vancouver, BC, Canada, 2022: 1–2. https://doi.org/10.1109/IPC53466.2022.9975568

[8] LIU H., MIAO P., XIAO Y., LIU C., ZHANG Z., WANG J., *High performance multi-junction VCSELs for LiDAR applications*, Proceedings of SPIE, Vol. 12020, Vertical-Cavity Surface-Emitting Lasers XXVI, 2022: 1202005. https://doi.org/10.1117/12.2609601

[9] Xiao Y., Wang J., Liu H., Miao P., Gou Y., Zhang Z., Deng G., Zhou S., *Multi-junction cascaded vertical-cavity surface-emitting laser with a high power conversion efficiency of 74%*, Light: Science & Applications, **13**(1), 2024: 60. https://doi.org/10.1038/s41377-024-01403-7

[10] Ghods A., Tatah K., Stocker M., Johnson K., *Scaling characteristics of multijunction VCSELs*, IEEE Journal of Selected Topics in Quantum Electronics, **31** (2), 2025: 1700907. https://doi.org/10.1109/JSTQE.2024.3467036

[11] Zhou X., Wang Y., Xun M., Pan G., Sun Y., Zhang R., Wu W., Wu S., Fei Y., Jiang X., Wu D., *Thermal properties of multi-junction cascade vertical cavity surface emitting lasers*, IEEE Transactions on Electron Devices, **71**(11), 2024: 6831–6837. https://doi.org/10.1109/TED.2024.3456769

[12] Liu Y., Huang Y., Zhong C., Zhang X., Zhang J., Hofmann W., Ning Y., Wang L., *VCSEL array thermal-distribution optimized by mesas rearrangement*, Optik, **186**, 2019: 443–448. https://doi.org/10.1016/j.ijleo.2019.04.113

[13] Zhong C.-Y., Zhang X., Liu D., Ning Y.-Q., Wang L.-J., *Enhanced thermal stability of VCSEL array by thermoelectric analysis-based optimization of mesas distribution*, Chinese Physics B, **26**(6), 2017, 064204. https://doi.org/10.1088/1674-1056/26/6/064204

[14] Wang J., Savidis I., Friedman E.G., *Thermal analysis of oxide-confined VCSEL arrays*, Microelectronics Journal, **42**(5), 2011: 820–825. https://doi.org/10.1016/j.mejo.2010.11.005

[15] Al-Omari A.N., Lear K.L., *VCSELs with a self-aligned contact and copper-plated heatsink*, IEEE Photonics Technology Letters, **17**(9), 2005: 1767–1769. https://doi.org/10.1109/LPT.2005.851938

[16] Yun Z.F., Yan L., Ting T.Z., Bo R.A., Jiang W., *High-power, multi-junction, 905 nm vertical-cavity surface-emitting laser with an AlGaAsSb electron-blocking layer*, Optics Letters, **48**(8), 2023: 2142–2145. https://doi.org/10.1364/OL.486922

[17] Blokhin S.A., Bobrov M.A., Maleev N.A., Kuzmenkov A.G., Sakharov A.V., Blokhin A.A., Moser P., Lott J.A., Bimberg D., Ustinov V.M., *Impact of a large negative gain-to-cavity wavelength detuning on the performance of InGaAlAs oxide-confined vertical-cavity surface-emitting lasers*, Proceedings of SPIE, Vol. 9381, Vertical-Cavity Surface-Emitting Lasers XIX, 2015: 93810W. https://doi.org/10.1117/12.2080942

[18] Yan W., Qiu P., Li M., Jia R., Wang Q., Zhao L., Kan Q., *Design and fabrication of high-power bottom-emitting 980-nm VCSELs*, [In] *Asia Communications and Photonics Conference 2021*, Optica Publishing Group, Shanghai, 2021: T4A.202. https://doi.org/10.1364/ACPC.2021.T4A.202

[19] Zhou X., Xun M., Pan G., Sun Y., Wang Y., Han C., Wu W., Wu S., Fei Y., Wu D., *High-power low-divergence single-mode multi-junction cascade VCSELs*, IEEE Transactions on Electron Devices, **71**(9), 2024: 5472–5476. https://doi.org/10.1109/TED.2024.3423801

[20] Michalzik R. [Ed.], *VCSELs: Fundamentals, Technology and Applications of Vertical-Cavity Surface-Emitting Lasers*, Springer Series in Optical Sciences, Vol. 166, Springer, Berlin, Heidelberg, 2013. https://doi.org/10.1007/978-3-642-24986-0

[21] Adachi S., *Lattice thermal conductivity of group-IV and III–V semiconductor alloys*, Journal of Applied Physics, **102**(6), 2007: 063502. https://doi.org/10.1063/1.2779259

[22] Lee H.K., Song Y.M., Lee Y.T., Yu J.S., *Thermal analysis of asymmetric intracavity-contacted oxide-aperture VCSELs for efficient heat dissipation*, Solid-State Electronics, **53**(10), 2009: 1086–1091. https://doi.org/10.1016/j.sse.2009.06.005

[23] Wang Z., Ning Y., Li T., Cui J., Zhang Y., Liu G., Zhang X., Qin L., Liu Y., Wang L., *High-Power Large-Aperture Bottom-Emitting 980-nm VCSELs With Integrated GaAs Microlens*, IEEE Photonics Technology Letters, **21**(4), 2009: 239–241. https://doi.org/10.1109/LPT.2008.2010510

[24] Calciati M., Tibaldi A., Bertazzi F., Goano M., Debernardi P., *Many-valley electron transport in AlGaAs VCSELs*, Semiconductor Science and Technology, **32**(5), 2017: 055007. https://doi.org/10.1088/1361-6641/aa66bb

[25] Vurgaftman I., Meyer J.R., Ram-Mohan L.R., *Band parameters for III–V compound semiconductors and their alloys*, Journal of Applied Physics, **89**(11), 2001: 5815–5875. https://doi.org/10.1063/1.1368156

[26] LIU C., LI Y., ZENG Y., *Progress in Antimonide Based III-V Compound Semiconductors and Devices*, Engineering, **2**(8), 2010: 617–624. https://doi.org/10.4236/eng.2010.28079

[27] SLIPCHENKO S.O., VINOKUROV D.A., PIKHTIN N.A., SOKOLOVA Z.N., STANKEVICH A.L., TARASOV I.S., ALFEROV ZH.I., *Ultralow internal optical loss in separate-confinement quantum-well laser heterostructures*, Semiconductors, **38**(12), 2004: 1430–1439. https://doi.org/10.1134/1.1836066

[28] BAVEJA P.P., KÖGEL B., WESTBERGH P., GUSTAVSSON J.S., HAGLUND Å., MAYWAR D.N., AGRAWAL G.P., LARSSON A., *Assessment of VCSEL thermal rollover mechanisms from measurements and empirical modeling*, Optics Express, **19**(16), 2011: 15490-15505. https://doi.org/10.1364/OE.19.015490

Received August 15, 2025
in revised form October 12, 2025